Tempered Point Clouds and OctoMaps: A Step Towards True 3D Temperature Measurement in Unknown Environments

Björn Zeise and Bernardo Wagner
Institute of Systems Engineering - Real Time Systems Group
Leibniz Universität Hannover, Appelstr. 9A, D-30167 Hannover, Germany
zeise | wagner @rts.uni-hannover.de

Abstract— **Although the generation of 3D temperature maps has become a frequently used technique, not only in search and rescue applications but also during inspection tasks, the remote measurement of a surface's true temperature is still a huge challenge. In this work, we face the problem of creating corrected 3D temperature maps in unknown environments without prior knowledge of surface emissivities. Using a calibrated sensor stack consisting of a 3D laser range finder and a thermal imaging camera, we generate *Tempered Point Clouds* (TPCs). With the help of the TPCs, we show how to perform a basic material classification, i.e. to make a distinction between metal and dielectric surface areas. For this purpose, we investigate measurements taken from different viewing angles. With the help of this approach, it is also possible to estimate corrected surface temperatures. The presented methods are evaluated making use of the OctoMap framework.**

I. INTRODUCTION

The need for environmental representations with temperature information (3D temperature maps) arises especially in the areas of search and rescue [1] and inspection [2]. Since thermography is affected by many influencing factors (e.g. material class, surface roughness, viewing angle), its application in unknown environments demands high amounts of interpretation and human intuition. This becomes a problem in situations where no human operator can be deployed, e.g. at disaster sites. Under these conditions, autonomously acting mobile robots are used for exploration (see [3] for a comprehensive survey). For reasons of self-preservation, those robots have to assess the current situation on their own.

This work tackles the problem of misinterpreted surface temperatures measured with a thermal imaging camera (TIC). Those misinterpretations originate from unknown surface emissivities – particularly on metal surfaces. Emissivity is a surface-specific property and closely linked to the temperature measured using a TIC. During exploration and inspection tasks, surface emissivities are most likely unknown, which results in erroneous temperature measurements. Depending on emissivity, the measurements taken by a TIC (also called apparent temperatures) may strongly differ from the true surface temperatures as determined using a contact thermometer. In our approach, we estimate corrected temperature values that are closer to the true temperatures by using the apparent temperatures and viewing angle information. In order to achieve this, we introduce so-called *Tempered Point Clouds* (TPCs) and show how to use them to generate corrected 3D temperature maps.

The remainder of this paper is organized as follows: In Section II, we give an overview on work related to temperature mapping, material classification and temperature correction. Section III introduces the concept of TPCs and gives an outline on how to generate tempered OctoMaps. In Sections IV and V, we present our approaches on basic surface material classification as well as on temperature correction. We close with an evaluation of the presented methods in Section VI and conclude our work in Section VII.

II. RELATED WORK

The projection of thermal images onto 3D surface structures has been covered in many publications in the last couple of years. In [2], the authors used a sensor stack consisting of a TIC and an RGB-D camera in order to create a 3D thermal map for inspection purpose. The authors of [4] investigated the temperatures of building façades. Just like in the work of [5], where 3D indoor environments were interpreted for energy efficiency, a 3D laser range finder (LRF) was used to acquire surface structures.

Material classification using thermal imaging information is not a well-known research topic. Nevertheless, it was recently investigated in [6]. The authors were able to classify 21 different materials using two different approaches. While one of the presented methods is based on water permeation, the other one uses a simple heating/cooling cycle. In contrast to our work, the camera operator has to manipulate the regarded object in order to perform a successful classification.

Two of our previous works faced the problem of temperature misinterpretations in thermal images, providing methods for temperature correction. In [7], we demonstrated the feasibility of temperature correction based on exploitation of the emissivity's angular dependency. The viewing angle information was provided manually and using an RGB-D camera, respectively. Details on how to calibrate a sensor stack consisting of a 3D LRF and a TIC in order to project thermal images onto point clouds were discussed in [8]. Using viewing angle information obtained from 3D data, we were able to estimate corrected surface temperatures of metal and dielectric areas.

In this paper – different from the results already presented in our previous works – we focus on the generation of 3D temperature maps in order to handle misinterpretations of thermal information. Before we estimate the material class and corrected temperatures, we fuse 3D range data and

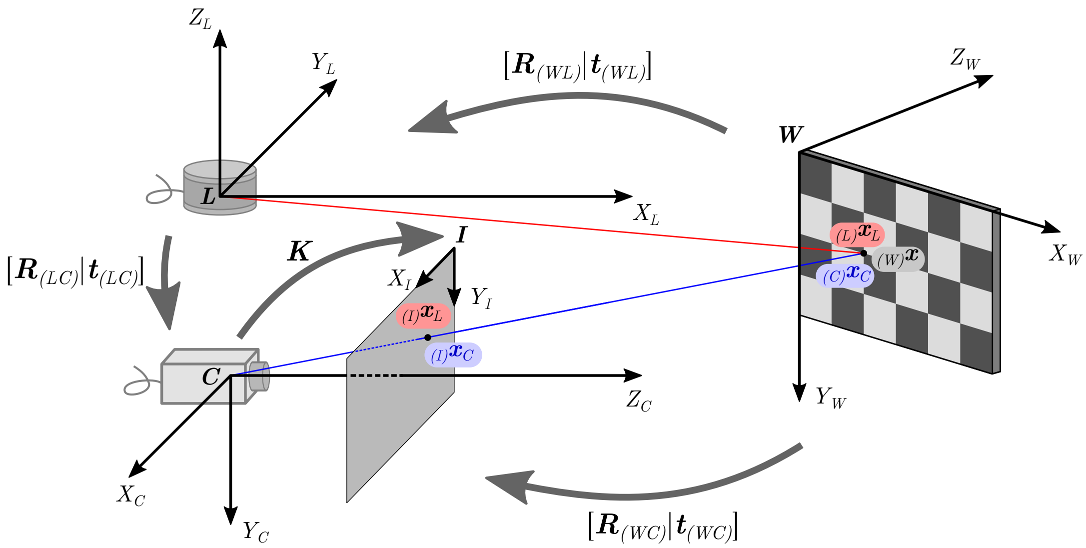

Fig. 1: Concept of temperature mapping and extrinsic calibration between LRF and TIC: With the help of a checkerboard pattern (defining the world coordinate system $\boldsymbol{W}$) a world point ${}_{(W)}\boldsymbol{x}$ (which can be detected by the LRF as ${}_{(L)}\boldsymbol{x}_L$ and by the TIC as ${}_{(C)}\boldsymbol{x}_C$) can be projected onto the image plane using the corresponding transformation matrices.

temperature information. This is in contrast to the methods mentioned above, where we directly corrected the thermal images pixel by pixel.

III. TEMPERED POINT CLOUDS

In order to differentiate conventional point clouds (consisting of points with three coordinates) from their tempered counterparts, we – from now on – denote point clouds consisting of points and according temperatures as TPCs. In order to project temperatures measured with a TIC onto 3D point clouds, the geometric constraints between the LRF and the TIC have to be determined. For a rigidly mounted sensor stack as considered in this work, a detailed description of a calibration method can be found in [8]. Instead of a trihedral calibration target, we use an individual calibration plane (heated checkerboard pattern) in this work. The subsequent section only gives a short overview on the LRF/TIC calibration procedure. For further information, the reader is referred to [8].

A. Extrinsic Calibration

Finding a transformation $\boldsymbol{T}_{(LC)} = \left[\, \boldsymbol{R}_{(LC)} \,|\, \boldsymbol{t}_{(LC)} \,\right]$ that transforms a laser point ${}_{(L)}\boldsymbol{x}_L$ given with respect to the laser coordinate frame $\boldsymbol{L}$ to a point ${}_{(C)}\boldsymbol{x}_L$ given with respect to the camera coordinate frame $\boldsymbol{C}$ is called *extrinsic calibration*. Fig. 1 outlines the geometric constraints that are relevant to the calibration procedure. The calibration method pursued here is based on [9]. Assuming the LRF's and TIC's intrinsics to be known, the extrinsic calibration parameters (rotation matrix $\boldsymbol{R}_{(LC)}$ and translation vector $\boldsymbol{t}_{(LC)}$) can be estimated by using least squares minimization:

$$\underset{\boldsymbol{T}_{(LC)}}{\operatorname{argmin}} \sum_{i=m}^{M} \sum_{n=1}^{N} \left(\hat{\boldsymbol{n}}_C^{(m)} \left(\boldsymbol{T}_{(LC)} \, {}_{(L)}\tilde{\boldsymbol{x}}_L^{(m,n)} \right) - d_C^{(m)} \right)^2 . \quad (1)$$

Eq. 1 matches laser points given with respect to $\boldsymbol{C}$ into the checkerboard plane that is given in Hesse normal form defined by a unit normal vector $\hat{\boldsymbol{n}}_C$ and a distance d_C. This plane is estimated using camera observations (corners of the checkerboard pattern) and RANSAC-based plane segmentation. Point ${}_{(L)}\tilde{\boldsymbol{x}}_L = \left({}_{(L)}\tilde{x}_L,\, {}_{(L)}\tilde{y}_L,\, {}_{(L)}\tilde{z}_L,\, 1 \right)^T$ is the homogeneous notation of point ${}_{(L)}\boldsymbol{x}_L$. The minimization is performed for N laser points per scan and M data pairs (laser scans and thermal images) in total.

A solution to the least squares minimization problem can be estimated using the Levenberg-Marquardt algorithm. Initial guesses for the calibration parameters are obtained by combining the individual transformations between the sensors and the calibration plane as follows:

$$\begin{aligned} &\left[\begin{array}{c|c} \boldsymbol{R}_{(LC)} & \boldsymbol{t}_{(LC)} \\ \hline \boldsymbol{0}^T & 1 \end{array}\right] \\ &\quad = \left[\begin{array}{c|c} \boldsymbol{R}_{(WL)} & \boldsymbol{t}_{(WL)} \\ \hline \boldsymbol{0}^T & 1 \end{array}\right]^{-1} \left[\begin{array}{c|c} \boldsymbol{R}_{(WC)} & \boldsymbol{t}_{(WC)} \\ \hline \boldsymbol{0}^T & 1 \end{array}\right] . \end{aligned} \quad (2)$$

For every observation, $\boldsymbol{T}_{(WL)}$ and $\boldsymbol{T}_{(WC)}$ can be calculated by applying plane segmentation on both the laser points that hit the calibration target and the detected checkerboard corners from the thermal image.

B. Temperature Mapping

Assuming the intrinsic camera matrix $\boldsymbol{K}$ to be known, a homogeneous laser point ${}_{(L)}\tilde{\boldsymbol{x}}_L$ with respect to $\boldsymbol{L}$ can be projected onto the TIC's image plane:

$$\begin{aligned} \tilde{w} \begin{pmatrix} u \\ v \\ 1 \end{pmatrix} &= \begin{pmatrix} {}_{(I)}\tilde{x}_L \\ {}_{(I)}\tilde{y}_L \\ \tilde{w} \end{pmatrix} \\ &= \boldsymbol{K} \left[\, \boldsymbol{R}_{(LC)} \,|\, \boldsymbol{t}_{(LC)} \,\right] {}_{(L)}\tilde{\boldsymbol{x}}_L . \end{aligned} \quad (3)$$

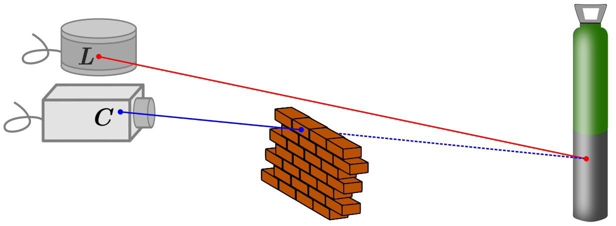

Fig. 2: Parallax error: A point that can be detected by the LRF is occluded with respect to the TIC.

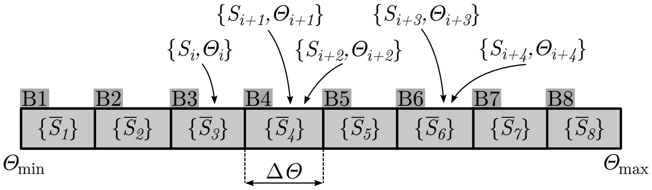

Fig. 3: Exemplary integration of detector signals S_i taken at viewing angles $\varTheta_i$ into a map cell's angle bins: For each bin (B1 to B8 in this case), an average detector signal $\overline{S}$, which is valid within a bin's range $\Delta\varTheta$, is calculated.

Dividing the resulting point ${}_{(I)}\tilde{\boldsymbol{x}}_L$ (with respect to the image coordinate system $\boldsymbol{I}$) by the scaling factor $\tilde{w}$, it can be transformed to image coordinates $(u, v)^T$. For the sake of simplicity, the camera image's distortion correction has been neglected in Eq. 3.

When projecting 3D laser points onto the TIC's image plane, some points might not be visible for the camera in case of an obstacle in front of the sensor stack. This is due to the (inevitable) distance between the sensors' optical centers. The phenomenon, which is commonly called *parallax error* [10], is depicted in Fig. 2. Parallax errors can be prevented by investigating the space between the camera frame's origin (with respect to $\boldsymbol{L}$) and the regarded laser point [5]. If there are other laser points in the line of sight, the current point's mapping procedure is skipped.

C. Map Generation

Map generation is based on an adapted version of the well-known OctoMap library [11]. In our approach, individual map cells are not only able to hold an occupancy probability but also several temperature measurements taken at different viewing angles. Those measurements (also called *detector signals*) are integrated into the map after calculating according viewing angles. Fig. 3 shows an exemplary integration of five detector signals into eight so-called *angle bins*. An angle bin is defined by its range

$$\Delta\varTheta = \frac{\varTheta_{\mathrm{max}} - \varTheta_{\mathrm{min}}}{J}, \tag{4}$$

where J is the total number of angle bins defined before map creation. The minimum and maximum viewing angles, $\varTheta_{\mathrm{min}}$ and $\varTheta_{\mathrm{max}}$, considered during map generation have to be chosen according to the viewing angle regions relevant to material classification (Section IV) and temperature correction (Section V).

The viewing angle for each point of a TPC is determined by calculating the angle between the vector pointing from ${}_{(L)}\boldsymbol{x}_L$ to the camera center and the surface normal in ${}_{(L)}\boldsymbol{x}_L$. Surface normal estimation was realized applying a PCA-based approach.

IV. MATERIAL CLASSIFICATION

In our approach, material classification (distinction between metal and dielectric surface points) is performed by exploiting the emissivity's viewing angle dependency. In this section, we provide an overview on the TIC's measurement principle, followed by an explanation of typical emissivity characteristics and model equations. This section is mainly based on one of our previous works. For further details, the reader is referred to [7].

The TIC does not directly provide temperature information. Instead, it pixel-wisely measures the radiation coming from a regarded surface. It then outputs a unitless detector signal S_{app} that can afterwards be converted to a meaningful temperature value [12]. For this purpose, the camera manufacturer provides the camera-specific constants R, B and F. In general, the object's true surface temperature T_{obj} is encoded using the following measurement formulas:

$$S_{\mathrm{app}} = \varepsilon\, S_{\mathrm{obj}} + (1-\varepsilon)\, S_{\mathrm{amb}} \tag{5}$$

with

$$S_{\mathrm{obj}} = \frac{R}{\exp\left(\frac{B}{T_{\mathrm{obj}}}\right) - F} \tag{6}$$

and

$$S_{\mathrm{amb}} = \frac{R}{\exp\left(\frac{B}{T_{\mathrm{amb}}}\right) - F}. \tag{7}$$

The apparent temperature that could be calculated using Eq. 6 or 7 with S_{app} instead of S_{obj} or S_{amb}, respectively, usually does not match the true surface temperature as determined using a contact thermometer. This is due to a surface-specific property called *emissivity* ε. Emissivity indicates, how well an object's surface emits (thermal) radiation compared to a black body of the same temperature [13].

Since an atmospheric influence of the medium between the TIC and the surface is neglected in Eq. 5, the apparent detector signal is the sum of a radiation part related to the object itself and a radiation part that originates from thermal ambient reflections on the object's surface.

A. Typical Emissivity Characteristics

Emissivity depends on influencing factors such as material class, surface roughness, viewing angle, wavelength and temperature [13]. The most characteristic dependencies are those on the material class and the viewing angle. Since the other dependencies cannot easily be neglected, some assumptions on our approach have to be made:

- The surfaces regarded in the work are assumed to be *optically smooth*, i.e. the largest surface impurities are smaller than the regarded wavelength.

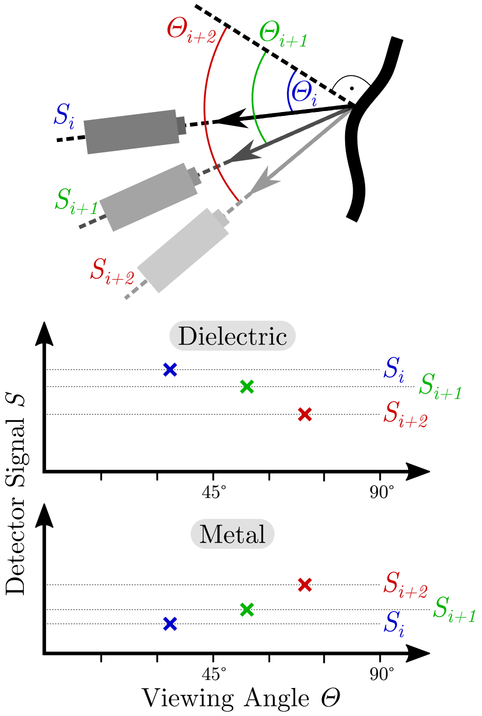

Fig. 4: Different detector signal characteristics of metals and dielectrics: According to Eq. 5, the detector signals S_i linearly depend on emissivity; taking several measurements (indicated by different colors) from multiple viewing angles Θ_i leads to the depicted graphs.

- Due to a lack of details on the TIC's signal processing chain that converts radiative power hitting a sensor element to the detector signal S_{app}, a wavelength-dependent reconstruction of temperatures T_{obj} and T_{amb} will not be possible.
- All measurements are taken in a static environment in terms of physical obstacles and surface temperatures.

Metals and dielectrics show fundamentally different emissivity characteristics depending on the viewing angle. Fig. 4 illustrates this behavior. Regarding metals, emissivity is low for small viewing angles. It rises up to a maximum for high viewing angles, just before falling down to zero at 90°. For dielectrics, emissivity is usually high up to viewing angles of 50°. After that, it monotonically falls down to zero.

In [14], equations for modeling emissivities of metals and dielectrics are presented. Those models depend on the viewing angle Θ as well as on two optical constants, namely the refractive index n and the extinction coefficient k. In our previous works ([7] and [8]), we found that no significant temperature improvement of dielectric surface points can be reached. This is due to the natively high emissivity of dielectrics, which results in only minor temperature misinterpretations. For that reason, we do not estimate corrected temperature values of dielectric surface areas in this work.

According to Kirchhoff's law of thermal radiation [15], emissivity ε equals absorption α. This leads to the following formulation:

$$\varepsilon = \alpha = 1 - \rho = 1 - \frac{\rho_\perp + \rho_\parallel}{2}. \tag{8}$$

In Eq. 8, ρ is the reflectivity which can be split into two parts. One of them is perpendicular polarized with respect to the plane of incidence ($\rho_\perp$); the other one parallel to it ($\rho_\parallel$). The equations modeling the reflectivity of metals are given as follows [14]:

$$\rho_{M,\perp} = \frac{(n - \cos\Theta)^2 + k^2}{(n + \cos\Theta)^2 + k^2} \tag{9}$$

and

$$\rho_{M,\parallel} = \frac{(n\cos\Theta - 1)^2 + (k\cos\Theta)^2}{(n\cos\Theta + 1)^2 + (k\cos\Theta)^2}. \tag{10}$$

Both the refractive index n and the extinction coefficient k depend on the regarded wavelength. Since the TIC used in our work does not measure at a specific wavelength but in a wavelength range between 7.5 µm and 14 µm, the true values for these properties cannot be determined. Nevertheless, we use the presented models in order to estimate corrected values for the surface and ambient temperatures. Eq. 9 and 10 can be simplified by setting n equal to k. This is commonly known as the *Hagen-Rubens relation* [16] and can be applied to measurements taken at wavelengths $\lambda > 6\,\mu\text{m}$.

B. Distinction between Metals and Dielectrics

Fig. 5 shows exemplary (real) measurements of individual surface points' detector signals S as functions of viewing angle Θ. As described before, the graphs for dielectric and metal points significantly differ. Since this difference is particularly visible for viewing angles $50° \leq \Theta \leq 80°$, we calculate a regression line for this range. In this case, the regression is not used to exactly fit the data points. Instead, the line is used to ascertain the monotonicity of the data points in the significant viewing angle range.

The distinction between a dielectric and a metal surface point is made by investigating the slope of the regression line. If the slope has a negative value (monotonically decreasing), the point is classified as *dielectric*; otherwise, if it has a positive value (monotonically increasing), the point is treated as *metal*.

V. TEMPERATURE CORRECTION

In order to estimate corrected values for the object temperature T_{obj}, a least squares minimization is performed for every individual map cell. Therefore, we use the measured detector signals saved in the angle bins in combination with the presented emissivity model equations. The minimization problem to be solved is the following:

$$\underset{\boldsymbol{p}}{\operatorname{argmin}} \sum_{i=1}^{I} \left(S_m^{(i)} - S_c^{(i)}(\boldsymbol{p}) \right)^2, \tag{11}$$

where $\boldsymbol{p} = \{k, T_{\text{obj}}, T_{\text{amb}}\}$ is the parameter vector to be optimized, I is the number of measurements taken into account, $S_m^{(i)}$ is the ith detector signal measurement and $S_c^{(i)}$ is the model of the detector signal according to Eq. 5 to 10.

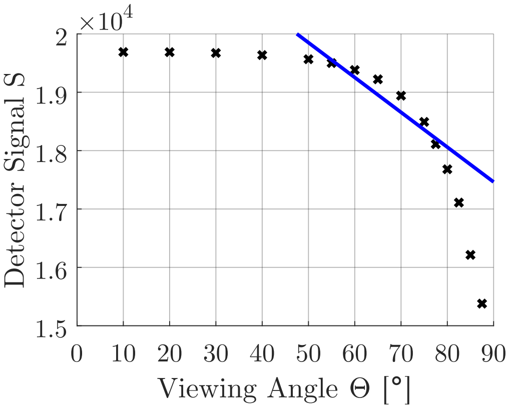

(a) Dielectric

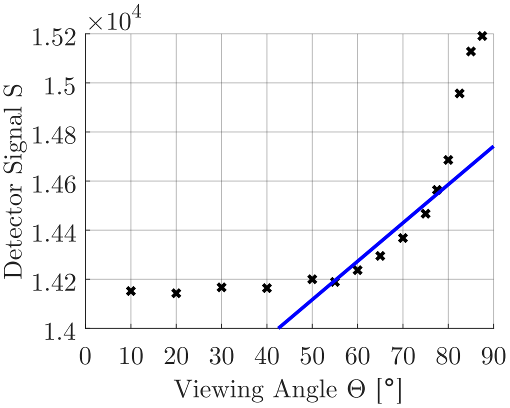

(b) Metal

Fig. 5: Exemplary measurements of detector signal S depending on viewing angle Θ for (a) dielectric and (b) metal surface points; blue line marks the regression line for measurements $50° \leq \Theta \leq 80°$.

VI. EVALUATION

Our approach was evaluated using a *Velodyne VLP-16* LRF and a *FLIR A655sc* TIC. The LRF provides 360° scans using 16 individual scan lines. Distance measurements can be taken up to a distance of 100 m with an accuracy of ± 3 cm. The LRF's vertical field of view (FOV) is 30°. During our experiments, measurements were taken with a rate of 10 Hz. The TIC works in the spectral range between 7.5 µm and 14 µm. The TIC's FOV is 45° × 34°. It provides images with a resolution of 640 × 480 pixels.

The experimental setup is depicted in Fig. 6. The sensor stack was pointing at a heated aluminum plate with some shapes made of duct tape on its surface. For proper data acquisition, the sensor stack was moved on a circular path around the plate. The aluminum plate was heated using a heat fan placed behind the plate. We used a contact thermometer to determine the temperatures of selected points (A and B) on the plate.

The sensor stack was calibrated using the method described in Section III-A. The calibration target is a heated aluminum plate with a checkerboard pattern on its front side. The pattern was created using (dielectric) duct tape. Due to the difference in emissivity of the blank and coated squares, the pattern is clearly visible in the thermal images.

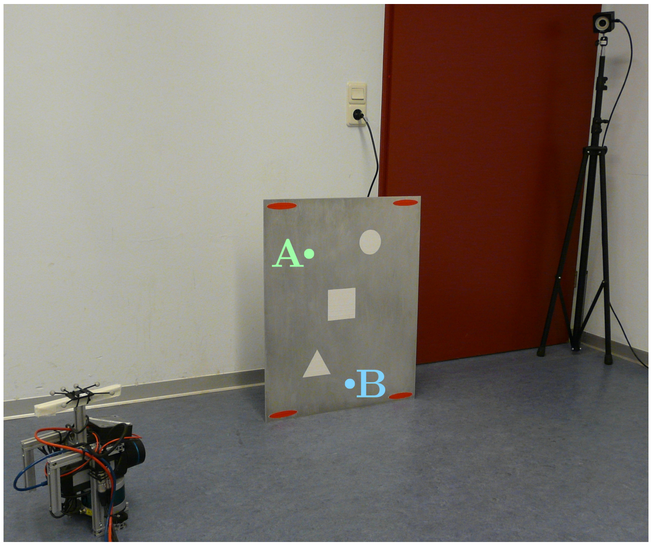

Fig. 6: Experimental setup: Sensor stack (bottom left) pointing at an aluminum plate (center, with dielectric shapes and temperature spots A and B); one of the tracking system's cameras can be seen on the right-hand side.

The sensor stack's pose was determined using an *OptiTrack Prime 13* tracking system with four camera modules. A tempered OctoMap with a resolution of 4 cm and 40 angle bins ($\Theta_{\text{min}} = 35°$ and $\Theta_{\text{max}} = 75°$) was created based on the method presented in Section III-C. Some of the resulting angle bins can be seen in Fig. 7.

A. *Material Classification*

Fig. 8 shows the OctoMap colored according to the detected material class. It can be seen that due to the low resolution of the map, the shapes do not completely match the real plate (see Fig. 6 for comparison). Nevertheless, every of the larger shapes on the plate is represented in the OctoMap.

B. *Temperature Correction*

In Fig. 9, the apparent temperatures of the aluminum plate are depicted. We calculated the average temperatures over all angle bins for this visualization. As stated before, the plate's true temperature (although not homogeneously distributed) was approx. 330 K at the lower part. Looking at the illustration, it is clear that the measurements taken with the TIC are heavily misinterpreted.

According to the method described in Section V, we estimated corrected temperature values for those regions that were identified as metals. Since dielectric surfaces natively have a high emissivity, no improvement for these surface regions was expected. For this reason, we focused on the temperature correction of the metal areas and simply integrated the average temperatures of dielectric regions from Fig. 9 into the corrected OctoMap. Fig. 10 shows the result of the temperature correction. For every map cell, least squares

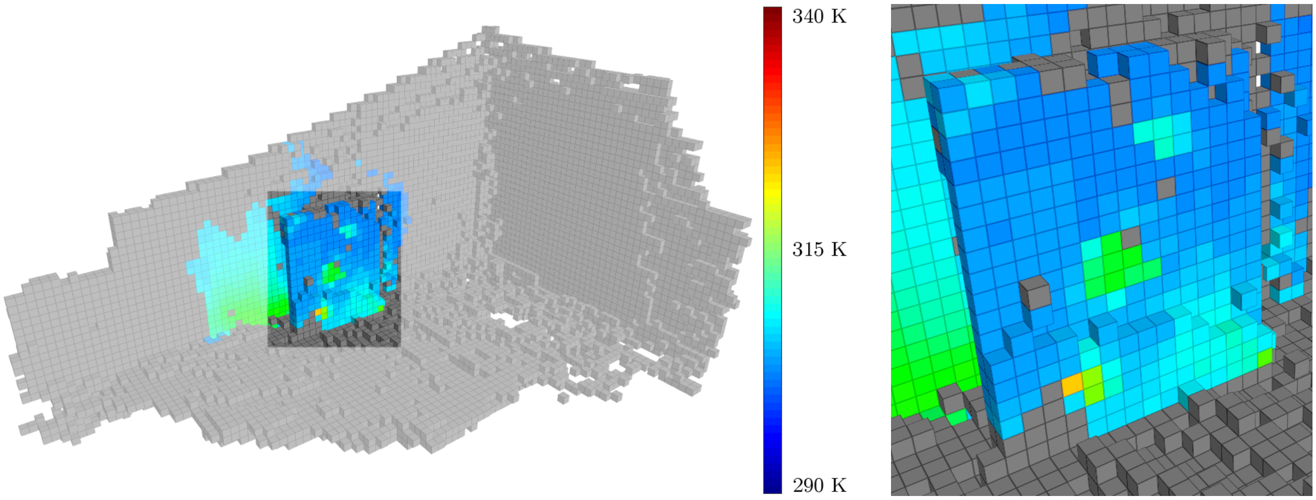

(a) Full, tempered OctoMap

(b) Temperatures at $\Theta = 45°$

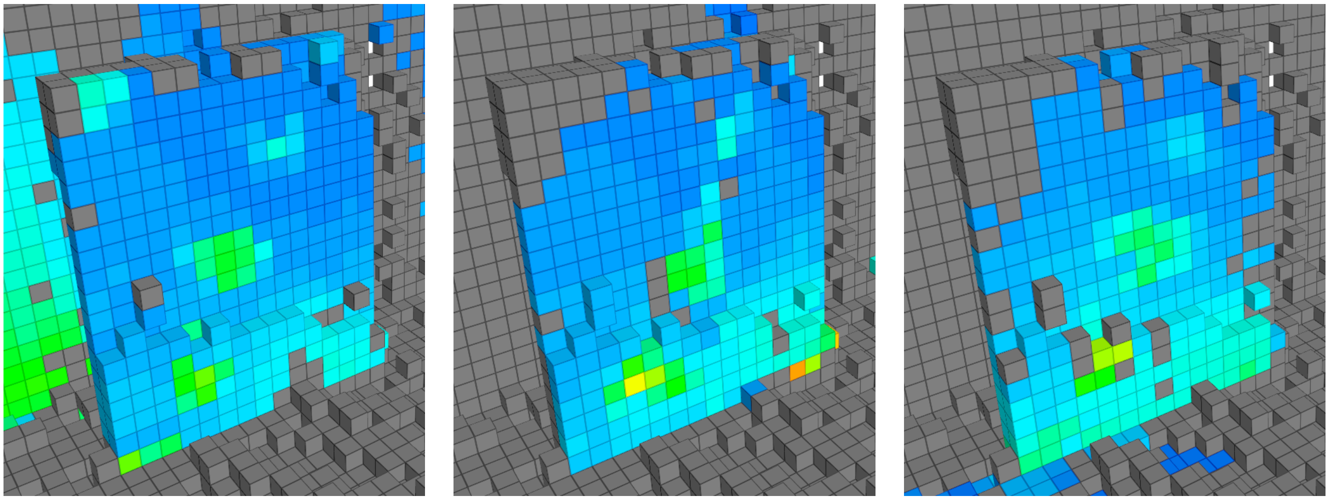

(c) Temperatures at $\Theta = 55°$

(d) Temperatures at $\Theta = 65°$

(e) Temperatures at $\Theta = 75°$

Fig. 7: Tempered OctoMap: (a) Full, tempered OctoMap and (b) to (e) enlargements of the heated plate at specific viewing angles.

minimization according to Eq. 11 was performed. Most of the estimated temperatures were satisfying. The uncolored, gray cells represent areas, for which we could not find a corrected temperature. This was due to bad optimization results, e.g. if the nonlinear solver exceeded reasonable temperature magnitudes. Finding the reasons for this will be the focus of future work.

In Fig. 6, two spots (A and B) on the surface are marked. The (true) temperatures of these spots were determined using a contact thermometer. In the upper region of the plate, a temperature $T_{\text{A,true}} \approx 308\,\text{K}$ was measured. The lower region had a temperature of $T_{\text{B,true}} \approx 333\,\text{K}$. The huge temperature inhomogeneity is due to the fact that the heat fan used during evaluation was rather small. Additionally, it was placed on the floor, which is why the lower measurement region is hotter than the upper one.

We compared the true temperatures with both the apparent temperatures and the estimated temperatures. For this purpose, we calculated the average temperatures of 10 map cells around the temperature spots A and B using Fig. 9 and Fig. 10. We determined the apparent temperatures ($T_{\text{A,app}} \approx 298\,\text{K}$ and $T_{\text{B,app}} \approx 302\,\text{K}$) as well as the corrected temperatures ($T_{\text{A,cor}} \approx 306\,\text{K}$ and $T_{\text{B,cor}} \approx 323\,\text{K}$). The estimated, corrected temperature values are much closer to the true surface temperatures than the apparent ones.

C. Discussion

During evaluation, the deviations between the apparent and the true temperatures of the selected spots A and B on a heated aluminum plate were measured as $\Delta T_{\text{A,app}} = 10\,\text{K}$ and $\Delta T_{\text{B,app}} = 31\,\text{K}$. After applying our method, the temperature errors reduced to $\Delta T_{\text{A,cor}} = 2\,\text{K}$ and $\Delta T_{\text{B,cor}} = 10\,\text{K}$, respectively. Although we were able to improve the temperatures, we have to mention some limitations and potential (future) challenges. First of all, we took our measurements in a thermally static environment, which means that we made sure that the reflections on the metal plate were homogeneous

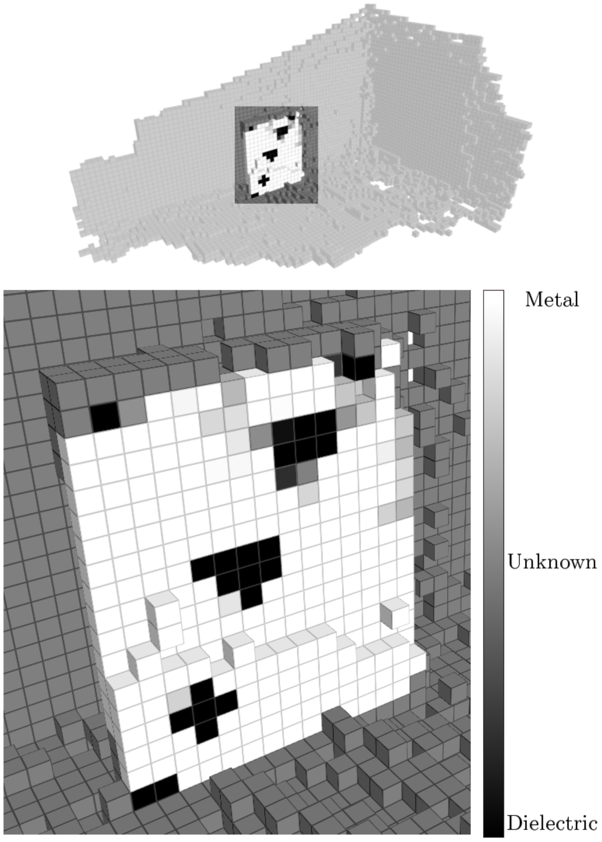

Fig. 8: Material classification result: Full OctoMap (top) showing metal (white) and dielectric (black) regions on the aluminum plate surface; enlargement of the plate on the bottom.

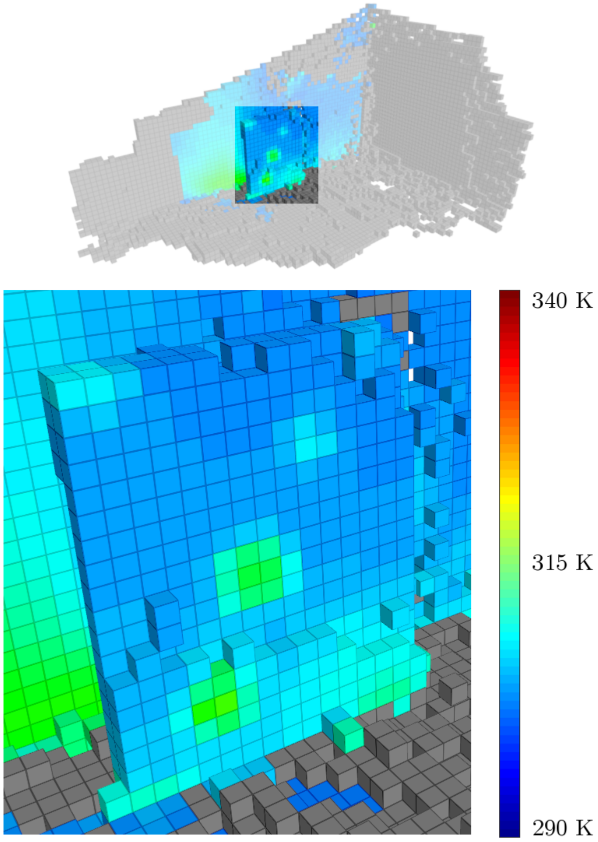

Fig. 9: Temperatures before correction step: Tempered OctoMap (top) and enlargement of the plate (bottom) with each map cell colored according to the depicted color bar; since the plate was partially heated to approx. 330 K, the apparent temperatures displayed here are heavily misinterpreted.

for most of the viewing angles ($T_{\text{amb}} = \text{const.}$). The influence of thermal reflections can be considered using appropriate reflections removal methods [8].

Another challenge are dielectric surface regions with high reflectivity caused by surface structures that are very smooth. If those surfaces do not have a high temperature, the influence of the reflected ambient temperature is too high to estimate a proper surface temperature (see Eq. 5). This could be avoided by setting a global minimum threshold for the detector signal to be taken into account.

Our method was evaluated using an aluminum plate. We did not investigate other metal surfaces. Since the general emissivity characteristic is the same for every metal, the portability of our approach to other metals should not pose a problem.

The nonlinear problem of temperature correction was solved by applying the Levenberg-Marquardt algorithm. We performed the optimization using lower and upper boundaries for all the parameters to be estimated (k, T_{obj} and T_{amb}). The initial values were chosen empirically. For the application in an unknown environment, it could be helpful to conduct the optimization step several times per map cell using different initial values. After that, the results should be assessed and the most trustworthy one should be visualized.

A last remark is on the usage of our method within the scope of mobile robots. Since we do not cover odometry estimation or localization in our work, we used highly accurate position data obtained from a tracking system in order to evaluate the system. Depending on the OctoMap resolution, which should not be too high, the utilization of Simultaneous Localization and Mapping (SLAM) algorithms for pose estimation (and OctoMap generation) should not cause difficulties.

VII. CONCLUSION

In this work, we addressed the problem of improving temperature values measured using a TIC in environments with unknown metal surface emissivities. Due to a typically low emissivity of metals, those apparent temperatures are usually interpreted as being much lower than the actual, true surface temperatures (as determined using a contact thermometer). Exploiting the emissivity's viewing angle dependency, we were able to distinguish between metal and dielectric surface areas and to estimate improved temperature values.

In order to achieve temperature correction, we first introduced the concept of TPCs. We then showed how to create TPCs with the help of an extrinsically calibrated sensor

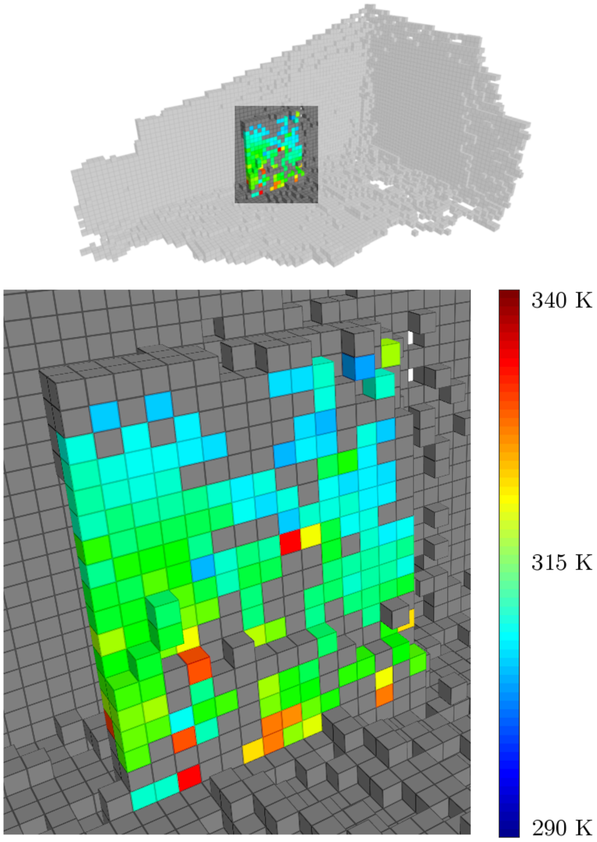

Fig. 10: Temperatures after correction step: Tempered OctoMap (top) and enlargement of the plate (bottom) with each map cell colored according to the depicted color bar; in comparison to Fig. 9, most temperatures are closer to their true values than before (for some map cells, the nonlinear solver was not able to find a reasonable result).

stack consisting of a 3D LRF and a TIC. Using TPCs, we generated tempered OctoMaps holding multiple angle bins, i.e. temperature measurements at different viewing angles. We showed that it is possible to identify the material class of heated surface regions by investigating the angle bins above a viewing angle of 50°.

In our experiments, we corrected the temperature measurements on metal surface regions by using a nonlinear minimization approach. We were able to reduce the temperature deviations (measurements without/with correction) that originate from unknown emissivity values by up to 67 %.

ACKNOWLEDGMENT

This work has partly been supported within H2020-ICT by the European Commission under grant agreement number 645101 (SmokeBot).

REFERENCES

[1] C. Schönauer, E. Vonach, G. Gerstweiler, and H. Kaufmann, "3D building reconstruction and thermal mapping in fire brigade operations," in *Proc. 4th Augmented Human Int. Conf.* Stuttgart (Germany): ACM, 2013, pp. 202–205.

[2] S. Vidas, P. Moghadam, and M. Bosse, "3D thermal mapping of building interiors using an RGB-D and thermal camera," in *Proc. 2013 IEEE Int. Conf. Robotics and Automation*. Karlsruhe (Germany): IEEE, 2013, pp. 2311–2318.

[3] R. R. Murphy, "Trial by fire [rescue robots]," *IEEE Robot. Automat. Mag.*, vol. 11, no. 3, pp. 50–61, 2004.

[4] D. Borrmann, J. Elseberg, and A. Nüchter, "Thermal 3D mapping of building façades," in *Intelligent Autonomous Systems 12*, ser. Advances in Intelligent Systems and Computing, S. Lee, H. Cho, K.-J. Yoon, and J. Lee, Eds. Berlin et al.: Springer, 2013, no. 193, pp. 173–182.

[5] G. G. Demisse, D. Borrmann, and A. Nüchter, "Interpreting thermal 3D models of indoor environments for energy efficiency," *J. Intelligent & Robotic Systems*, vol. 77, no. 1, pp. 55–72, 2015.

[6] P. Saponaro, S. Sorensen, A. Kolagunda, and C. Kambhamettu, "Material classification with thermal imagery," in *Proc. IEEE Conf. Computer Vision and Pattern Recognition*. Boston (MA, USA): IEEE, 2015, pp. 4649–4656.

[7] B. Zeise, S. P. Kleinschmidt, and B. Wagner, "Improving the interpretation of thermal images with the aid of emissivity's angular dependency," in *Proc. 2015 IEEE Int. Symp. Safety, Security, and Rescue Robotics*. West Lafayette (IN, USA): IEEE, 2015, pp. 1–8.

[8] B. Zeise and B. Wagner, "Temperature correction and reflection removal in thermal images using 3D temperature mapping," in *Proc. 13th Int. Conf. Informatics in Control, Automation and Robotics*, vol. 2. Lisbon (Portugal): Scitepress, 2016, pp. 158–165.

[9] Q. Zhang and R. Pless, "Extrinsic calibration of a camera and laser range finder (improves camera calibration)," in *Proc. IEEE/RSJ Int. Conf. Intelligent Robots and Systems*, vol. 3. Sendai (Japan): IEEE, 2004, pp. 2301–2306.

[10] J. Rangel, S. Soldan, and A. Kroll, "3D thermal imaging: Fusion of thermography and depth cameras," in *Proc. 12th Int. Conf. Quantitative InfraRed Thermography*. Bordeaux (France): QIRT Council, 2014.

[11] A. Hornung, K. M. Wurm, M. Bennewitz, C. Stachniss, and W. Burgard, "OctoMap: An efficient probabilistic 3D mapping framework based on octrees," *J. Autonomous Robots*, vol. 34, no. 3, pp. 189–206, 2013.

[12] M. Martiny, R. Schiele, M. Gritsch, A. Schulz, and S. Wittig, "In situ calibration for quantitative infrared thermography," in *Proc. 3rd Int. Conf. Quantitative InfraRed Thermography*. Stuttgart (Germany): QIRT Council, 1996, pp. 3–8.

[13] M. Vollmer and K.-P. Möllmann, *Infrared thermal imaging*, 1st ed. Weinheim (Germany): Wiley-VCH, 2010.

[14] J. R. Howell, R. Siegel, and M. P. Mengüç, *Thermal radiation heat transfer*, 5th ed. Boca Raton (FL, USA): CRC Press, 2011.

[15] G. Kirchhoff, "Ueber das Verhältniss zwischen dem Emissionsvermögen und dem Absorptionsvermögen der Körper für Wärme und Licht," *Annalen der Physik*, vol. 185, no. 2, pp. 275–301, 1860.

[16] E. Hagen and H. Rubens, "Über Beziehungen des Reflexions- und Emissionsvermögens der Metalle zu ihrem elektrischen Leitvermögen," *Annalen der Physik*, vol. 316, no. 8, pp. 873–901, 1903.